Mesoscale correlation structure with single cell resolution during visual coding

Yiyi Yu, Jeffrey N. Stirman, Christopher R. Dorsett, Spencer L. Smith
University of California Santa Barbara; University of North Carolina Chapel Hill

Neural circuitry represents sensory input with patterns of spiking activity. Across brain regions, initial representations are transformed to ultimately drive adaptive behavior. In mammalian neocortex, visual information is processed by primary visual cortex (**V1**) and multiple higher visual areas (**HVAs**). The interconnections of these brain regions, over which transformations can occur, span millimeters or more. Shared variability in spiking responses between neurons, called "noise correlations" (**NCs**), can be due to shared input and/or direct or indirect connectivity. Thus, NCs provide insight into the functional connectivity of neuronal circuits. In this study, we used subcellular resolution, mesoscale field-of-view two-photon calcium imaging to systematically characterize the NCs for pairs of layer 2/3 neurons across V1 and four HVAs (areas LM, LI, AL and PM) of mice. The average NCs for pairs of neurons within or across cortical areas were orders of magnitude larger than trial-shuffled control values. Within-area NCs declined with distance between neurons, but for inter-area NCs the distance-dependence was mixed. NCs were higher for neuron pairs with similar tuning (i.e., signal correlations). To explore tuning-specific NCs in finer detail, we used an unbiased clustering approach to classify neurons based on their responses to orientated gratings. This analysis revealed biases in the coverage of spatiotemporal frequency space across HVAs, and relationships between orientation tuning biases and spatiotemporal frequency preferences. Using the resulting functional groupings, we found group-specific within-area and inter-area patterns of NCs, indicating functionally-specific subnetworks. Overall, these results reveal new principles for the functional organization and correlation structure across multiple cortical areas, which can inform and constrain computational theories of cortical networks.

Introduction

Navigating the environment, detecting predators, and recognizing mates are natural behaviors of mammals that can depend upon sophisticated visual perception. Visual information is encoded and abstracted through multiple interconnected brain areas, which span millimeters in the mouse[1]. These interconnections, both within and between brain areas, are critical components underlying brain functions. Anatomical tracing studies of flies[2] and mice[3], have provided insights into basic neuronal wiring principles. However, anatomical connectivity is insufficient for understanding the circuit interactions of an active brain, and the relationships between function and connectivity. Thus, in this study we investigated the functional circuit connectivity structure at millimeter scale.

Neuronal responses vary on nominally identical trials. The trial-to-trial variability of responses is correlated in a neuronal population. This shared variability between pairs of neurons can be quantified, and is called noise correlation (**NCs**)[4]. The structure of NCs is rooted in the architecture of the neuronal circuit, e.g., shared bottom up and top down input, as well as recurrent connections[5–11]. The dynamics of NCs during stimulus onset[12], locomotion[13], circuit plasticity[14] and brain state change[9,15,16] can provide an important window into neuronal connectivity principles, which are an important component of the functional properties of neural circuits[11]. The structure of NCs have provided important constraints on neuronal network models of stimulus encoding[9,17–19], motor behavior[18], attention[20] and decision making[21]. For example, a recurrent network model with spatially structured connectivity[22] was inspired by the distance-dependent structure of NCs[23,24], which was uncovered in an attention modulation study in the monkey visual cortical system[25,26]. In most studies, NCs were measured only in pairs of relatively closely positioned pairs of neurons in a population, often within a single cortical region, due to technical limitations of recording methods. Thus, the structure of longer distance, inter-area correlations remains unclear. Some studies have managed to record neuronal activity at single neuron resolution in two or more areas simultaneously by multielectrode recording[26–29], and these studies have provided important insights in NCs. However, they are typically limited to 20-60 neurons in each area and are typically contaminated by multi-neusronal activity, and these limit the analyses, leaving larger scale principles of NCs between single neurons uninvestigated. To address this issue, we have developed a large field-of-view two-photon microscope with temporally multiplexed imaging beams[30], which can measure neuronal activity in hundreds of neurons at subcellular resolution, across millimeters of cortex[30].

In mouse visual cortex, the primary visual area (**V1**) and multiple higher visual areas (**HVAs**) are involved in visual processing[1,31–33]. V1 and HVAs response to diverse visual stimuli[34]. HVAs vary in spatial and temporal frequency selectivity[31,32,34], and receive specialized input from V1[35,36]. V1 and HVAs are densely interconnected[36,37], and form segregated inter-area feedforward and feedback connections[38–40], indicating hierarchical structure between V1 and HVAs[41,42].

To assess the functional interactions among neurons in V1 and HVAs, we systematically characterized the structure of NCs between pairs of neurons, both within individual visual areas and between visual areas. We found a strong relationship between tuning and NCs, which could overcome distance-dependent declines in NCs in cases of inter-area pairs of neurons. Along the way, we also identified trends in functional clustering among neurons based on their orientation tuning and spatiotemporal frequency preferences. Together, these findings provide insights into circuit structure for the emergence of functional specialization of HVAs.

Results

1. Multi-region two-photon calcium imaging from V1 and HVAs

To measure neuronal activity, we used multi-region population calcium imaging of L2/3 neurons in V1 and four HVAs (lateromedial, **LM**; laterointermediate, **LI**; anterolateral, **AL**; and posteromedial, **PM**) using a multiplexing, large field-of-view two-photon microscope with subcellular resolution developed in-house[30] (**Fig.**

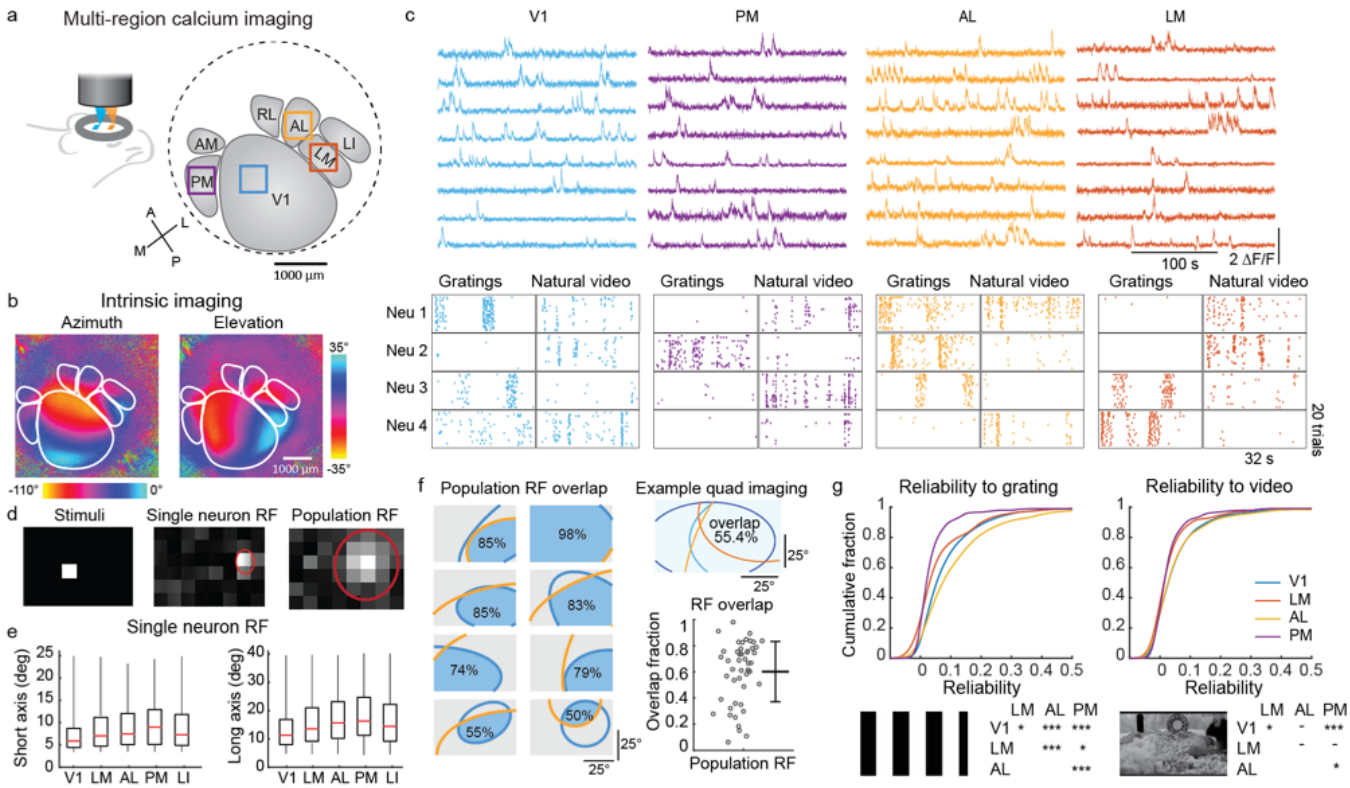

Figure 1. Multi-region two-photon calcium imaging. (**a**) Cartoon of multi-region two-photon imaging of mouse V1 and HVAs, using custom wide field-of-view microscope. Example imaging session of simultaneous recording session of V1, LM, AL and PM. Blue and orange square indicate a 500 µm^2 imaging window. (**b**) Example intrinsic signal imaging of mouse visual areas. (**c**) Top: example neuropil corrected calcium traces of multi-region calcium imaging to drifting grating stimuli. Bottom: spike raster plots of example neurons from V1, PM, AL and LM responding to drifting grating stimuli at 8 directions (SF: 0.04 cpd, TF 2Hz, 0 ~ 315°) and to naturalistic video. (**d**) Left: moving patch of vertical drifting grating (left) was used for RF mapping. The size of the moving patch is about 8°. Example RF of single neuron (middle) and population neurons (right) were fit with 2D Gaussian (red). (**e**) Short and long axis of the Gaussian profile of single neuron RF of all tested HVAs neurons are longer than that of V1 (short, $p = 9.6 \times 10^{-53}$; long, $p = 4.9 \times 10^{-43}$; $N_{V1} = 4093$; $N_{LM} = 713$; $N_{AL} = 529$; $N_{PM} = 326$; $N_{LI} = 318$; One-way ANOVA with Bonferroni correction). (**f**) Left: example population RFs of simultaneously imaged populations. Blue and orange contours indicate Gaussian profile of population RF of neurons from different visual areas, and blue shade indicates the overlap region of population RF of two simultaneously imaging regions. Values indicate the fraction of overlap. Upper right: example population RF of the quartic-region imaging shown in (**a**). Lower right: summarize the fraction of population RF overlap of individual experiments (gray circle). Error bar indicate the mean and standard division. (**g**) The cumulative fraction of reliability of V1 and three HVAs to drifting gratings at SF 0.04 cpd, TF 2 Hz ($p = 2.4 \times 10^{-23}$; $N_{V1} = 1449$; $N_{LM} = 166$; $N_{AL} = 307$; $N_{PM} = 293$) and naturalistic video ($p = 2.7 \times 10^{-6}$; $N_{V1} = 2177$; $N_{LM} = 175$; $N_{AL} = 334$; $N_{PM} = 354$). Reliability was computed at 500 ms bins. The star chart at the bottom indicates the significance of the one-way ANOVA test with Bonferroni correction (* $p < 0.05$; ** $p < 0.01$; *** $p < 0.001$).

1a). Mice expressed the genetically encoded calcium indicator GCaMP6s[43,44] in cortical neurons. We located V1 and HVAs of each mouse using retinotopic maps obtained by intrinsic signal optical imaging[32,45] (**Fig. 1b**). We imaged neurons in 2 – 4 cortical visual areas simultaneously (**Fig. 1a, c**). We typically imaged neurons in V1 and one or more HVAs. Up to 500

neurons (V1: 129 ± 92; HVAs: 94 ± 72; mean ± SD.) were recorded per imaging region (500 x 500 μm^2). The imaging regions were matched for retinotopy (**Fig. 1c**), so that the neurons in the simultaneously imaged areas had overlapping receptive fields (**RFs**). Calcium signals were used to infer probable spike trains for each neuron (*Methods*; **Supplementary Fig. 1a**). Neurons in V1 and HVAs exhibited similar instantaneous firing rates (**Supplementary Fig. 1b**). We mapped RFs for individual neurons and populations using small patches of drifting gratings (**Fig. 1d**). Neurons in HVAs (LM, AL, PM and LI) had significantly larger RFs than V1 neurons (**Fig. 1e**). Population RFs for a 500 x 500 μm^2 imaging region of HVAs covered significantly larger portions of visual space than that of V1 (**Supplementary Fig. 1c**), as expected given their differing magnification factors[46]. The overlap of population RFs confirmed that simultaneously imaged cortical areas (V1 and HVAs), each containing ~10^2 neurons, responded to stimuli in the same region of visual space (**Fig. 1f**).

Using the multi-region imaging paradigm, we recorded reliably responding neurons from V1 and HVAs to both drifting gratings (8 direction at 0.05 cycles/° and 2 Hz) and naturalistic videos (a mouse eye-level view navigating around a mouse home cage) (**Fig. 1c**). The firing reliability to drifting gratings was highest in AL (0.11 ± 0.1; mean ± S.D.), while slightly lower in V1 (0.08 ± 0.09; mean ± S.D.) and LM (0.06 ± 0.09; mean ± S.D.), and lowest in PM (0.036 ± 0.05; mean ± S.D.) (**Fig. 1g**). The firing reliabilities for responses to naturalistic videos were similar in V1 and AL (V1, 0.052 ± 0.09), and were lower in LM and PM (0.029 ± 0.05; mean ± S.D.) (**Fig. 1g**). Consistent with previous studies[34], we found that neuron responsiveness differed between areas and depended on stimulus. Among reliably firing neurons (reliability > 0.08), over half of the neurons responded to drifting gratings (V1, 54%; LM, 69%; AL, 67%; PM, 61%), and a partially overlapping group of neurons responded to naturalistic video (V1, 87%; LM, 71%; AL, 62%; PM, 70%) (**Supplementary Fig. 1d**). Some neurons responded to both stimulus types, and this portion was smallest in AL and largest in PM (V1, 40%; LM, 39%; AL, 29%; PM, 50%; $p = 5.6 \times 10^{-11}$, One-way ANOVA with Bonferroni correction; **Supplementary Fig. 1d**). These reliable responses provide a basis for further analysis.

In a separate set of experiments, we examined the response selectivity of V1 and HVAs to drifting gratings of various parameters and naturalistic video using the metric lifetime sparseness. V1 and HVAs responded sparsely to both sine-wave drifting gratings (72 conditions: 8 directions x 3 spatial frequencies x 3 temporal frequencies) and naturalistic videos. The lifetime sparseness of responses to drifting gratings was slightly higher in V1 than HVAs (LM, AL, PM and LI), and the sparseness of responses in AL was the lowest ($p = 2.5 \times 10^{-35}$; ANOVA with Bonferroni correction; **Fig. 2a**). The sparseness of responses to naturalistic videos were similar in V1, LM and AL, and slightly lower in PM ($p = 0.0004$; One-way ANOVA with Bonferroni correction; **Fig. 2a**). Thus, neurons in simultaneously imaged areas (V1 and HVAs) in this dataset encode stimuli in similar regions of visual space, can respond reliably to stimuli, and exhibit high lifetime sparseness.

2. Within-area and inter-area noise correlation

Next, we systematically characterized NCs of pairs of neurons within and across V1 and multiple HVAs (LM, LI, AL, and PM). We computed the NCs of pairs of neurons within individual cortical areas (within-area NC), and NCs for pairs of neurons where the two neurons are in different cortical areas (inter-area NC) (**Fig. 2b**). NCs were computed using spike counts within 1 s bins, similar to previous work with electrophysiology[4,23]. Both within- and in4 ter-area NCs had wide distributions (range: -0.2 – 0.6). The mean NCs across a population was positive and at least five times larger than NCs computed after shuffling the trials (5 – 20-fold, 25 – 75% quantile; **Fig. 2c**). Although the NC estimation of individual neuron pairs was noisy (**Supplementary Fig. 2a**), both simulation and experimental data suggested that the estimation of the population mean NC converges with increasing numbers of neurons (95% confidence

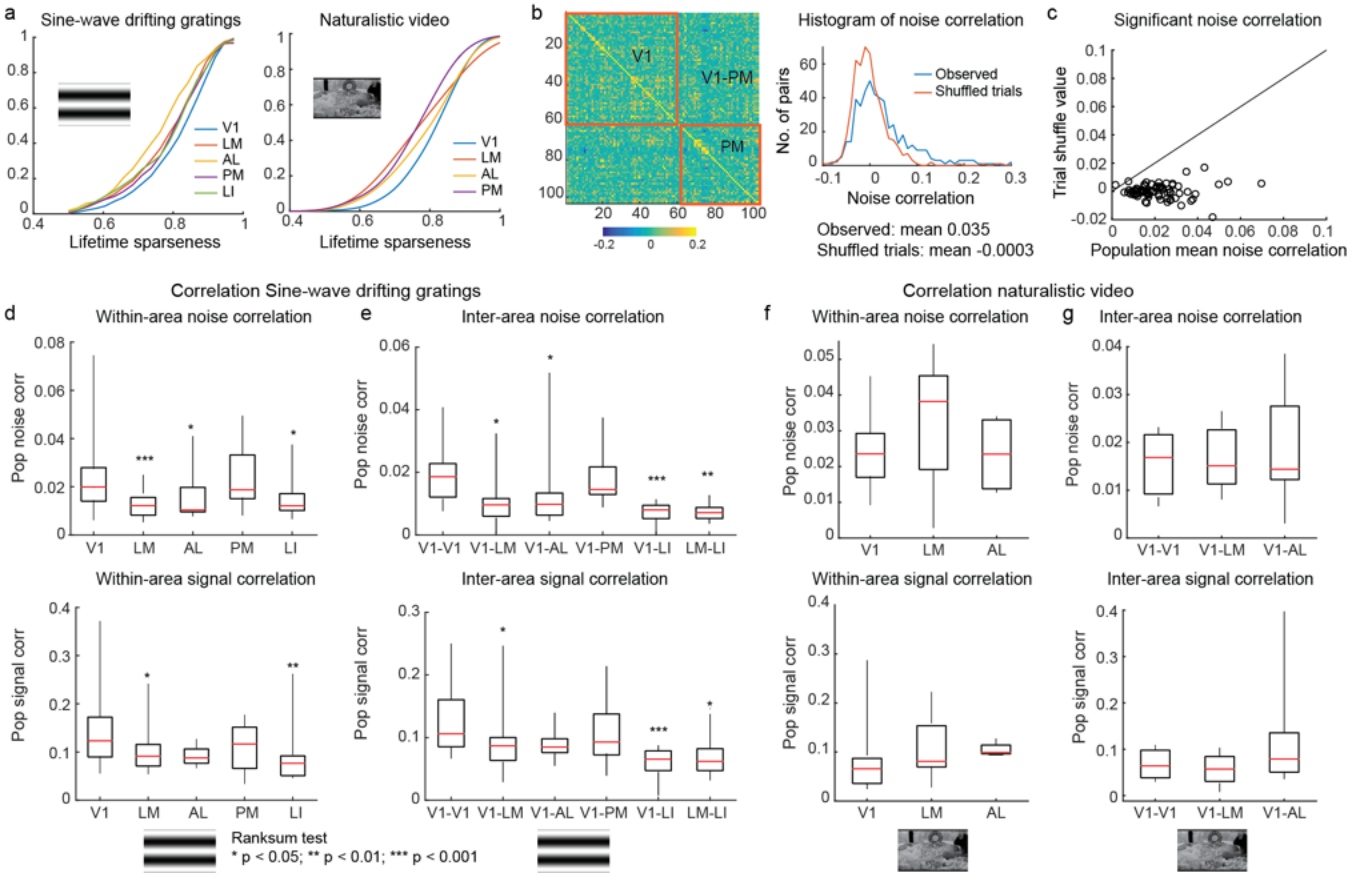

Figure 2. Within- and inter-area noise correlations. (**a**) Cumulative distribution of lifetime sparseness of V1 and HVAs to Sine-wave drifting gratings (left) and naturalistic video (right). Lifetime sparseness was computed is reliable firing neurons (reliability > 0.08). The lifetime sparseness to drifting gratings of V1 was significantly larger than all tested HVAs, and the sparseness of AL was significantly lower than other areas (N_{V1} = 3264, N_{LM} = 947, N_{AL} = 380, N_{PM} = 243, N_{LI} = 170; p = 2.5 x 10^{-35}). The lifetime sparseness to naturalistic video of V1 was significantly higher than PM, but not LM and AL (N_{V1} = 712, N_{LM} = 35, N_{AL} = 101, N_{PM} = 46; p = 0.0004; p-value of one-way ANOVA with Bonferroni correction). (**b**) Left: example covariance matrix of a quadratic recording of V1 and PM. Right: NC of an imaging session computed by trial aligned (blue) and trial shuffled data (red). (**c**) Population mean NC is significantly larger than the residual correlation after trial shuffling. Gray dots indicate the value of individual experiments. (**d**) Boxplot of population mean within-area NC (upper) and signal correlation (lower) to gratings (compare to V1, NC: P_{LM} = 0.0003, P_{AL} = 0.016, P_{PM} = 0.9, P_{LI} = 0.019; signal correlation: P_{LM} = 0.03, P_{AL} = 0.05, P_{PM} = 0.25, P_{LI} = 0.009; N_{V1} = 48, N_{LM} = 16, N_{AL} = 12, N_{PM} = 10, N_{LI} = 8). (**e**) Boxplot of population mean inter-area NC (upper) and signal correlation (lower) to gratings. (NC: $P_{V1\text{-}LM}$ = 0.016, $P_{V1\text{-}AL}$ = 0.03, $P_{V1\text{-}PM}$ = 0.75, $P_{V1\text{-}LI}$ = 0.0008, $P_{LM\text{-}LI}$ = 0.0016; signal correlation: $P_{V1\text{-}LM}$ = 0.039, $P_{V1\text{-}AL}$ = 0.05, $P_{V1\text{-}PM}$ = 0.26, $P_{V1\text{-}LI}$ = 0.0008, $P_{LM\text{-}LI}$ = 0.015; $N_{V1\text{-}V1}$ = 13, $N_{V1\text{-}LM}$ = 21, $N_{V1\text{-}AL}$ = 16, $N_{V1\text{-}PM}$ = 19, $N_{V1\text{-}LI}$ = 11, $N_{LM\text{-}LI}$ = 8). (**f**) Boxplot of population mean within-area NC (upper) and signal correlation (lower) to naturalistic video (NC, p = 0.19; signal correlation: p = 0.76; N_{V1} = 29; N_{LM} = 10; N_{AL} = 6). (**g**) Boxplot of population mean inter-area NC (upper) and signal correlation (lower) to naturalistic video (NC, p = 0.07; signal correlation, p = 0.52; $N_{V1\text{-}V1}$ = 5; $N_{V1\text{-}LM}$ = 12; $N_{V1\text{-}AL}$ = 9). (**f, g**) p-values of one-way ANOVA.

interval is ~0.002 with 50 neuron pairs, **Supplementary Fig. 2b, c**). Thus, NCs at the population level are roughly an order of magnitude greater than trial-shuffled control values and are reliably estimated.

Within- and inter-area NCs linearly increased with neuron spike count to both drifting gratings and naturalistic videos (**Supplementary Fig. 3a, b**). NCs were also positively modulated by neuron reliability to both stimulus types

(**Supplementary Fig. 3c, d**). To avoid biases in correlation estimates due to neuron responsiveness (characterized by spike count and reliability), we computed population mean NCs and signal correlations (**SCs**, which is the tuning similarity) using subpopulations of reliably firing neurons with matched spike count distribution across visual areas (*Methods*).

Neurons with similar tuning properties shared higher NCs[4,23,24,47] (but see ref. [7] for an exception). Consistently, we observed that both within- and inter-area NCs increased with SCs for drifting grating stimuli (**Supplementary Fig. 4a, b**). The within-area NCs of V1 and HVAs increased with SCs at a similar rate, which was slightly larger than the increasing rate of corresponding inter-area NCs (**Supplementary Fig. 4c**).

We found that lateral areas (LM and LI) exhibited lower within-area NCs and SCs than V1 to drifting gratings, while PM were not different from V1 (**Fig. 2d**). Inter-area NCs of V1-LM, V1-AL, V1-LI, and LM-LI were significantly lower than that of V1-V1 (simultaneously imaged, non-overlapping regions of V1); while V1-PM was not detected to be different from V1-V1 (**Fig. 2e**). Similarly, the inter-area SCs of V1-V1 was significantly larger than the inter-area SCs between V1 and HVAs, except PM and AL (**Fig. 2e**). The differences in inter-area correlations between V1-V1 and V1-HVAs were significant over a broad range of reliabilities and spike counts (**Supplementary Fig. 3a, c**). Thus, within-area and inter-area NCs and SCs can exhibit area-specific structure.

The area-specific NCs and SCs were modulated by the statistics of the visual stimuli. V1, LM, and AL exhibited similar NCs during stimulation with naturalistic videos, as well as similar SCs (**Fig. 2f**). Among these areas, LM, but not V1 and AL, exhibited larger NCs to naturalistic stimuli than that to drifting gratings (gratings: 0.012 ± 0.007; naturalistic: 0.029 ± 0.01, mean ± S.D.; $p = 0.011$; Wilcoxon rank sum test). The SC of V1 was lower to naturalistic stimuli, compared to drifting gratings (gratings: 0.12 ± 0.075 naturalistic: 0.088 ± 0.07, mean ± S.D.; $p = 1.6 \times 10^{-5}$; Wilcoxon rank sum test). On the other hand, during naturalistic video stimulation, the inter-area NCs of V1-AL was increased (gratings: 0.01 ± 0.005; naturalistic: 0.024 ± 0.016, mean ± S.D.; $p = 0.017$; Wilcoxon rank sum test), and it was not differed from the NCs of V1-V1 and V1-LM (**Fig. 2g**). Overall, multiple features of correlation structure can be modulated by the visual stimulus.

Within-area NCs increased when mice were anesthetized (**Supplementary Fig. 4d**), consistent with prior reports. Here, we extended this finding to inter-area NCs, which also increased (**Supplementary Fig. 4d**). In summary, we observed that the structure of correlations for pairs of neurons within and across areas exhibits area-specific features and can be modulated by the visual stimulus. This suggests that there could be neural circuits whose efficacy at driving downstream firing depends on the cortical area and stimulus.

3. Interactions between tuning groups of V1 and HVAs

Given the strong relationship between SCs and NCs (**Supplementary Fig. 4a, b**), we sought to characterize SCs (i.e., tuning similarity), in greater detail. Mouse V1 and HVA neurons exhibit diverse tuning preferences to drifting grating stimuli[31,32]. These tuning preferences could be distributed continuously across the population, or neurons might be organized into functional groups of tuning preferences. If the latter is the case, then NCs within and across functional groups could provide insights into functional wiring principles of neural circuitry.

First, we characterized the tuning properties of V1 and HVA neurons. After pooling all V1 and HVA neurons imaged, we used a Gaussian Mixture Model (GMM)-based approach to identify functional groupings of neurons. This process partitioned neurons into six groups by their joint selectivity to SF, TF, and direction (*Methods*, **Fig. 3a, Supplementary Fig. 5, 6**). Groups 1, 2, and 3 all prefer low TF (1-2 Hz), but vary in their SF preference: low SF (0.02 cpd), medium SF (0.05 cpd) and high SF (0.19 cpd) respectively. Groups 4, 5 and 6 all prefer high TF (8 Hz), but again vary in their SF preference: low SF, medium SF, and high SF respectively. The groups varied in other ways as well. Neurons in Groups 1, 2, and 3 (low TF) tend to have narrow tuning for SF,

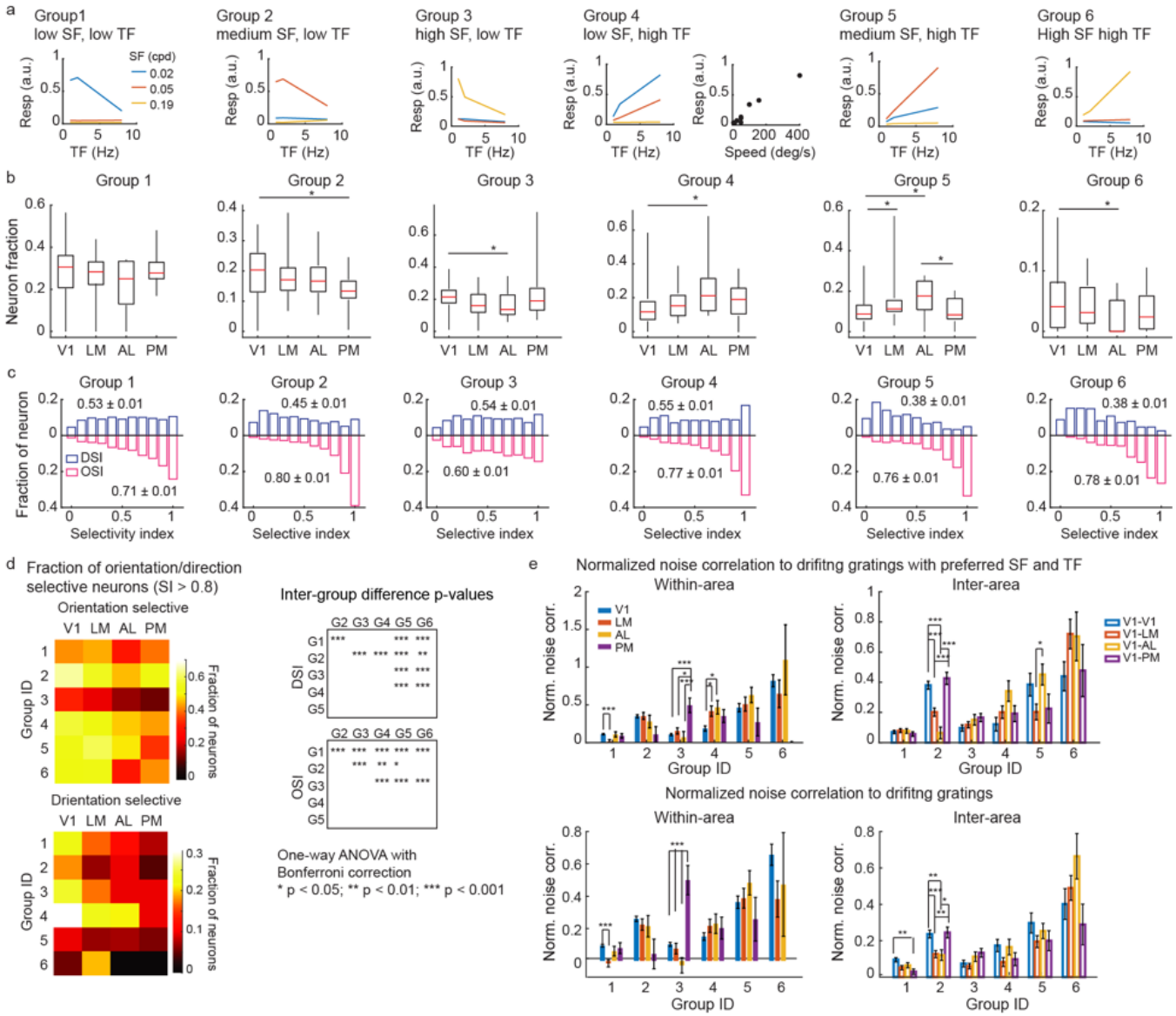

Figure 3. Spatial-dependence of tuning properties. (**a**) Define GMM tuning Group 1-6. Line figures show normalized responses to joint combination of SF and TF. Dot plot in group 4 shows normalized response to the speed of drifting grating. (**b**) Fraction of neurons of V1 and HVAs belong to each group. Stars indicate the significance rank sum test (number of experiments: N_{V1} = 54, N_{LM} = 21, N_{AL} = 13, N_{PM} = 11, N_{LI} = 8). (**c**) Histograms of DSI (purple bars) and OSI (pink bars) of tuning groups. Inserted values indicate mean ± se. (**d**) Left: Heatmap shows the fraction of orientation (OSI > 0.8, left) and direction selective neurons (DSI > 0.8, right) of each tuning group in V1, LM, AL and PM. Right: Star chart indicates the significance of inter-group comparison of DSI and OSI. Reported p-values of one-way ANOVA with Bonferroni correction. (**e**) Normalized within-area (left) and inter-area (right) NC of each tuning groups to drifting gratings concatenated over all SF-TF conditions (bottom) and to drifting gratings with preferred SF and TF. Normalized NC is computed by compensating the population mean and variance of NC. Stars indicate the significance of One-way ANOVA with Bonferroni correction (*, $p < 0.05$; **, $p < 0.001$; ***, $p < 0.0001$). The number of neuron pairs in each group of each area is greater than 100, except Group 6 of AL and PM.

indicated by how they typically responded to only one of the three SFs. By contrast, Groups 4 and 5 had broader SF tuning. Moreover, Group 4 (low SF, high TF) was the only group that exhibited clear trends with respect to the overall drift speed of the grating stimulus (drift speed = TF/SF, and is measured in deg/s), with higher responses at higher speeds. These groupings were robust in the data (*Methods*, **Supplementary Fig. 7**).

The GMM-based grouping revealed cortical area differences in SF-TF tuning (**Fig. 3b**). While all visual areas had a similar fraction of neurons tuned to low TF and low SF (Group 1), fractions in other groups varied by area. LM had a larger fraction of neurons tuned to medium SF, high TF (Group 5). AL had larger fraction of neurons tuned to high TF, and low to medium SF (Groups 4 and 5), and a smaller fraction of neurons tuned to high SF (Groups 3 and 6). PM had a smaller fraction of neurons tuned to medium SF (Groups 2 and 5). Overall, there is a trend of increasing preferred TF from posterior-medial to anterior-lateral visual cortex (Pearson correlation, A→P, cor = -0.25, p =0.015, M→L, cor = 0.36, p = 0.0004), and a trend of increasing preferred SF from anterior to posterior visual cortex (Pearson correlation, cor = 0.35, p = 0.0005) (**Supplementary Fig. 8a, b**).

We computed the orientation selectivity index (OSI) and direction selectivity index (DSI) for neurons in each tuning group (**Fig. 3c, d**). All six groups contained orientation and direction selective neurons with diverse direction preferences. The OSI and DSI of V1 and HVAs were jointly modulated by SF and TF. Neurons tuned to high SF and low TF (Group 3) exhibited lower OSI than all of the other groups (Group 3: mean OSI = 0.6; other groups ranged from 0.71 – 0.80; p < 0.0001, one-way ANOVA with Bonferroni correction; **Fig. 3c**). About 18% of neurons in Group 3 were orientation selective (OSI > 0.8), while about 40 – 50% of neurons in other groups were orientation selective.

The GMM analysis was performed using neurons pooled from all cortical areas, so it is possible that there would be area-specific trends for neurons in a particular group. However, Group 3 neurons were consistently low OSI, in V1 and all tested HVAs (**Fig. 3d, Supplementary Fig. 8e**). V1 and LM had similar orientation selectivity in all tuning groups. However, AL exhibited lower OSI and had fewer orientation selective neurons in Group 1-3 and 6, but not in Group 4 and 5 compared to other areas (**Fig. 3d, Supplementary Fig. 8e**). PM had a smaller fraction of orientation selective neurons in Group 5 (**Fig. 3d**).

The direction selectivity of Groups 5 and 6 (high TF, low-medium SF) were lower than those of Groups 1 – 4, consistently in V1 and HVAs (Group 5, 6, DSI 0.38; other groups, DSI 0.45 ~ 0.54; p < 0.0001, one-way ANOVA with Bonferroni correction; **Fig. 3c, d; Supplementary Fig. 8e**). However, LM had a larger fraction of direction selective neurons in Group 6 (V1, 5%; LM, 19%; **Fig. 3d)**. V1 exhibited higher direction selectivity than HVAs in majority tuning groups, expect Group 6. AL and PM exhibited low direction selectivity in all tuning groups, except Group 4 of AL (**Fig. 3d, Supplementary Fig. 8e**). LM had similar direction selectivity with V1 in majority groups, but in Group 2 LM had lower direction selectivity (**Fig. 3d, Supplementary Fig. 8e**).

In addition, the preferred directions were unbiasedly represented in V1 and HVAs, except high SF groups (Group 3 and 6) of AL and PM biased to upward, or cardinal directions (**Supplementary Fig. 8c**). We did not observe clear spatial trend in preferred direction within V1. Indeed, V1 neurons within a small neighborhood (150 μm^2) exhibited diverse direction preference (**Supplementary Fig. 8d**). Overall, this robust grouping analysis demonstrated a previously undescribed organization in functional diversity in V1 and HVAs. SF, TF, and orientation tuning are not evenly distributed over a continuum, but instead exhibit specific groupings and biases.

After identifying tuning groups in V1 and HVAs, we characterized the within- and inter-area interactions between tuning groups. In general, tuning groups exhibited strong group-specific NCs, for both within and inter-area neuron pairs (**Supplementary Fig. 9a, b**). Since V1 and HVAs vary in their mean NCs to drifting gratings (**Fig. 2d, e**), and this can complicate the interpretation of inter-group NCs, we computed normalized NCs, normalizing individual areas by

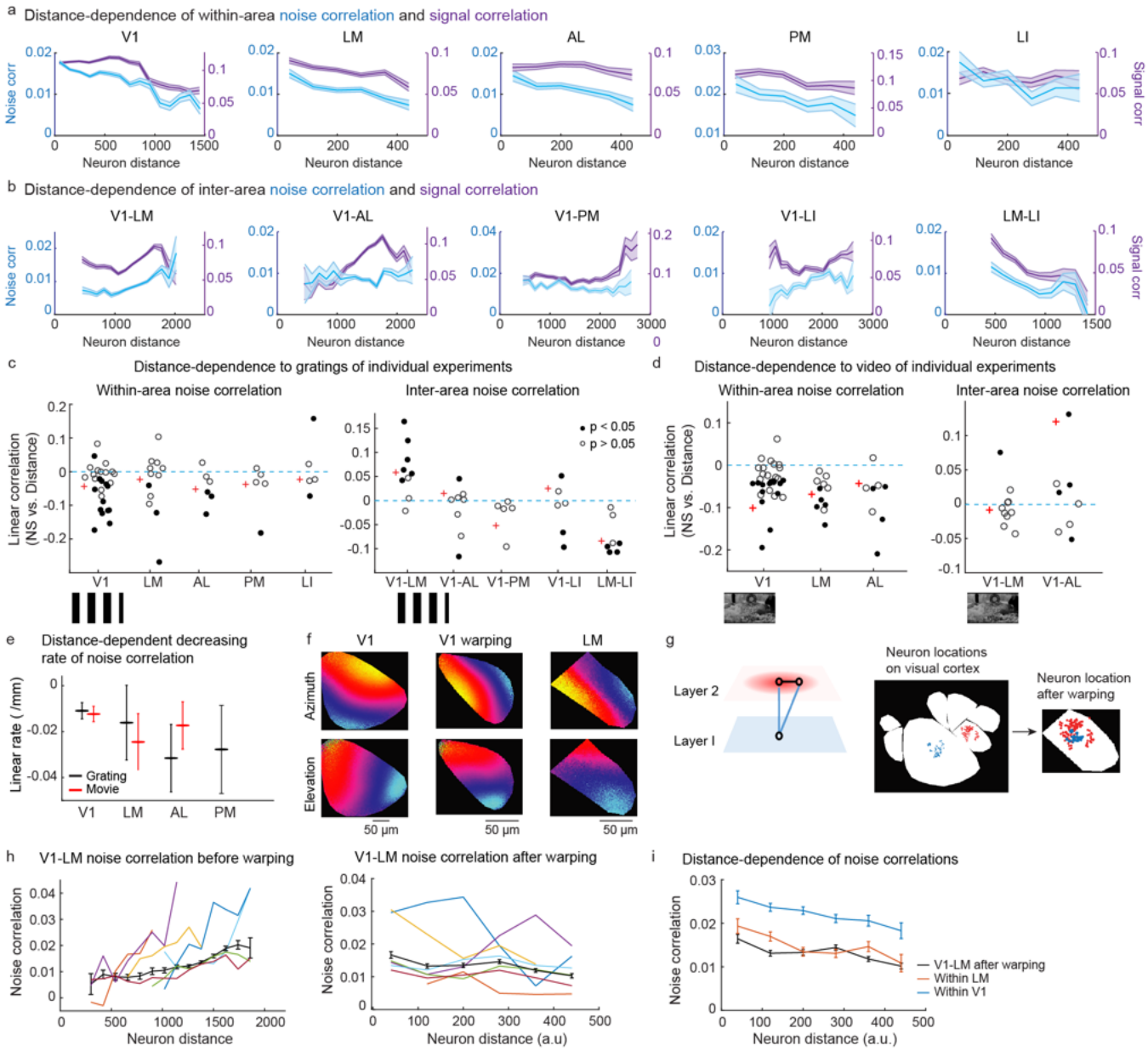

Figure 4. Distance-dependence of noise correlation. (**a**) Distance-dependence of within-area NC (blue) and signal correlation (purple) to sine-wave drifting gratings (NC: V1, cor = -0.044, p = 3.5 x 10^{-40}; LM, cor = -0.026, p = 0.0009; AL, cor = -0.05, p = 7.7 x 10^{-7}; PM, cor = -0.048, p = 0.0026; LI, cor = -0.025, p = 0.17. Signal correlation: V1, cor = -0.03, p =9.8 x 10^{-24}; LM, cor = -0.036, p = 4.4 x 10^{-6}; AL, cor = -0.028, p = 0.0067; PM, cor = -0.048, p = 0.005; LI, cor = -0.037, p = 0.047; Pearson correlation). (**b**) Distance-dependence of inter-area NC (blue) and signal correlation (purple) to sine-wave drifting gratings (NC: V1-LM, cor = 0.058, p = 5.5 x 10^{-41}; V1-AL, cor = 0.013, p = 0.02; V1-PM, cor = -0.05, p = 2.8 x 10^{-14}; V1-LI, cor = 0.028, p = 0.0007; LM-LI, cor = -0.08, p = 3.2 x 10^{-15}; Signal correlation: V1-LM, cor = 0.073, p = 2.6 x 10^{-64}; V1-AL, cor = 0.073, p = 1.7 x 10^{-35}; V1-PM, cor = -0.01, p = 0.047; V1-LI, cor = 0.056, p = 8.2 x 10^{-12}; LM-LI, cor = -0.084, p = 2.8 x 10^{-53}; Pearson correlation). (**a, b**) Solid lines indicate mean values and shaded areas indicate standard error of mean. Each distance bin contains >50 data points. (**c, d**) Pearson correlation coefficients between NCs and neuron distance of individual experiments to sine-wave drifting gratings (**c**) and naturalistic video (**d**). Open circles indicate insignificant Pearson correlation coefficients and solid circles are significant values. (**e**) Linear coefficients of a linear fitting to the mean NC vs. neuron distance function. Error bars are 95% confidence interval of the linear coefficients. (**f**) Example affine transformation of ISOI maps. The left shows the original V1 map, the middle is the V1 map after affine transformation and the right is the original LM map. (**g**) Left, cartoon

the population mean and variance of NCs (*Methods*). Group 3 exhibited pronounced area-specific differences for within-area neuron pairs, while Group 2 exhibited marked area-specific differences for inter-area pairs (**Fig. 3e**). In Group 3, PM exhibited significantly higher normalized NCs than V1, LM and AL to both preferred and non-preferred stimuli (PM, 0.5 ± 1.3; V1 0.1 ± 1.2; Mean ± S.D.; $p = 1.3 \times 10^{-6}$; one-way ANOVA with Bonferroni correction). In Group 2, the inter-area normalized NC of V1-V1 and V1-PM was significantly larger than that of V1-LM and V1-AL to both preferred and non-preferred stimuli ($p = 4.7 \times 10^{-5}$; one-way ANOVA with Bonferroni correction). PM had a lower fraction of Group 2 (medium SF, low TF) neurons and a relatively higher fraction of Group 3 (low TF, high SF) neurons (**Fig. 3b**). The Group 2 of PM exhibited high interaction with V1, but not within itself; while Group 3 of PM exhibited higher interaction within itself, but only moderately interacted with V1. This interaction pattern of PM may indicate that the emergence of Group 3 of PM was independent of V1, while the emergence of Group 2 of PM was more likely dependent on V1. On the other hand, the normalized NCs of V1-AL to preferred stimuli in high TF groups (Group 4~6) were higher than that of low TF groups (Group 1~3) ($p < 0.0001$, t-test). PM and AL exhibited high interaction with non-overlapping V1 tuning groups, (i.e., low TF-medium SF groups to PM, while high TF-medium SF to AL), consistent with the non-overlapping projection pattern of V1 to PM and AL[38]. Over all, the area-specific interaction pattern of tuning groups further supported that visual cortical neurons form discrete functional groups with specific correlation structures within and across cortical areas.

4. Distance-dependence of in- and inter-areal noise correlation

Prior studies have provided differing accounts of how NCs vary with the distance between neurons. Studies that reported low mean NCs found no distance-dependence of noise correlations[10,48], while studies that reported higher mean NCs found that noise correlations declined with neuron distance[23,24]. In the current study, we characterized the distance-dependence of NCs within and between multiple visual cortical areas. Note that all distances are lateral distances across cortex. In general, the NCs of neurons within a visual area declined with increasing distance (this was true when using either drifting gratings or naturalistic videos; **Fig 4a, c, d**). The distance-dependent decrease of within-area NCs was not different among V1, LM, AL and PM, for either drifting gratings or naturalistic videos (linear decreasing rate of NC -0.02 ± 0.009 (mm^{-1}); mean ± S.D.; **Fig. 4e**). SCs of V1, LM, AL and PM, exhibited significant distance-dependent decreases (**Fig. 4a**). However, the distance-dependence of within-area NCs were not explained by the decrease in SCs, as the partial correlation between NCs and neuron distance, even when conditioned on both SC and firing rate, was significant within V1, LM, AL and PM (Drifting gratings partial correlation: V1, $r = -0.03$, $p < 0.0001$; LM, $r = -0.0173$, $p = 0.025$; AL $r = -0.050$, $p < 0.0001$; PM, $r = -0.048$, $p = 0.0019$). We did not observe a distance-dependent pattern of NCs in LI (**Fig. 4a, c**). The distance-dependence of NCs, independent of tuning similarity and firing rate, suggested distance-dependent recurrent connections between neurons within visual areas (V1, LM, AL and PM).

In contrast to largely monotonic changes in NCs within areas, inter-area NCs exhibited region-specific distance-dependence patterns that were often non-monotonic (**Fig. 4b-d**). To drifting gratings, inter-area signal correlations of V1-LM, V1-AL, and V1-LI pairs increased with distance; and V1-PM and LM-LI pairs declined with neuron distance (**Fig. 4b**). The distance-dependent trend of V1-LM, V1-PM and LM-LI persisted after controlling for SCs and firing rate

of two recurrent layer with aligned retinotopic map. Right: neuron location on the visual cortex before and after warping. (**h**) Distance-dependent increasing of V1-LM NC to sine-wave drifting gratings before (left) and after retinotopic warping (right). Individual experiments with significant distance-dependence are in shown in colored curves. The black curve shows the population mean and standard error (Pearson correlation, before warping, cor = 0.066, $p = 1.3 \times 10^{-36}$; after warping, cor = -0.026, $p = 3.8 \times 10^{-7}$). (**i**) Distance-dependence of within-area NCs of paired recorded V1 and LM, and inter-area NC of V1-LM after retinotopic warping.

(partial correlation: V1-LM, r = 0.045, p = 8.2 x 10^{-26}; LM-LI, r = -0.048, p = 6.4 x 10^{-6}; V1-PM, -0.05, p = 9 x 10^{-15}). New did not find a distance-dependent change for V1-AL and V1-LI after controlling for SCs and firing rate. The distance dependence of V1-LM was significant in individual experiments to drifting gratings, but not to naturalistic videos (**Fig. 4c, d**). These diverse relationships between distance and NCs for inter-area neuron pairs could be due to the topography of retinotopic maps.

In mouse visual cortex, the orientation of retinotopic maps vary by HVA. To examine whether the distance-dependent increase of V1-LM NCs to drifting gratings could be explained by retinotopy (**Fig. 1c**), we aligned V1 and LM retinotopy by affine transformations of intrinsic signal maps of V1 to match those of LM (*Methods*, **Fig. 4f**). After retinotopic warping, V1 and LM were treated as two layers with aligned retinotopies (**Fig. 4g**) such that neurons with nearby receptive field locations in visual space also have small inter-area neuronal distances. We found the distance-dependent increase of V1-LM NCs to drifting gratings was eliminated after retinotopy alignment (**Fig. 4h**). Instead, the inter-area NC between V1 and LM exhibited a distance-dependent decrease after warping (Linear correlation, cor = -0.26, p = 3 x 10^{-6}; **Fig. 4f**), similar to the trends found for within-area NCs in V1 and LM (**Fig. 4i**). This shows that retinotopic alignment is a major driver of NCs which can overcome simple distance-dependent increases. Similarly, after retinotopic alignment the V1-LM NCs to naturalistic video didn't exhibit significant distance-dependence (Linear correlation, p = 0.47 ± 0.35; mean ± SD.).

Discussion

These results reveal features of the structure of correlations in mouse visual cortex at the mesoscale with single cell resolution, from V1 to HVAs. The data set also uncovered a functional clustering of neurons, which also exhibits specific correlational structure both within and across visual cortical areas. These new details of neural activity correlations can provide clues to wiring principles and areal specialization.

Noise correlation and network modeling

Detailed knowledge of the structure of NCs can be used to constrain neuronal network models. Accounts of NC structure is discordant among previous studies[4]. Some groups reported low NC values, around 0.001 – 0.01[10,48], in favor of a balanced excitation-inhibition network with random connectivity, called an asynchronous network[10]. Other groups have reported higher NC values of ~0.1 – 0.4[23,24,49] (see ref. [4] for a review), which cannot be predicted by the asynchronous network model. The population mean NC values reported in the current study (0.01 – 0.1) were in the intermediate range of previously reported values[4,10,47,48]. The asynchronous network model predicts spatially uniform NCs, which is inconsistent with experimental findings of NC decay with neuron distance in monkey V1 and V4[23,24]. This form of NC was well captured by a neuronal network model with distance-dependence connectivity[22,25]. In the current study, we found that NCs of neurons within a cortical area as well as V1 and LM neuron pairs after retinotopic alignment, exhibited distance-dependent decay. Moreover, the decay rate is similar for both-within and inter-area correlations. These findings favor a neuronal network model with spatially (and functionally[50,51]) structured connectivity.

Emergence of areal specialization

Mouse HVAs are specialized for distinct spatial-temporal frequency bands[31,32,52]. Consistent with a previous paper[52], we found that mouse visual cortical neurons exhibited tuning biases that were easily clustered (rather than continuous), and the SF and TF preference of mouse visual areas were segregated. For example AL responded the best to high TF and low SF drifting gratings, while PM responded the best to high SF low TF drifting gratings. In the current study, we revisited functional specialization of LM, AL and PM using unbiased classification methods, and using this method we characterized the joint tuning properties of HVAs to SF, TF and direction. Consistent with previous findings[31,32], we found that AL responded the best to high TF and low to medium SF band, PM responded the best to high SF and low SF brand, and LM responded the best to low to medium SF and high TF band (**Fig. 3b; Supplementary Fig. 6b**). In addition, we found AL responded to a speed tuning group the best comparing to other tested visual areas (**Fig. 3b**). Moreover, we found the orientation and direction tuning was modulated jointly by SF and TF non-continuously. Neurons tuned to high SF low TF band exhibited extremely low orientation selectivity, and neurons tuned to high TF and medium to high SF; as well as neurons tuned to medium SF and low TF exhibited low direction selectivity (**Fig. 3c**). Meanwhile, the tuning specific direction/orientation selectivity pattern varied among HVAs (**Fig. 3d**). In summary, the data set revealed the area-specific joint tuning preferences on SF, TF, and direction.

It remains unclear how tuning properties emerge in HVAs. Mouse HVAs receive functionally specialized V1 projections, and these could be important for the areal specialization[35,38]. However, one study has shown that thalamic input from superior colliculus, but not V1 input, is essential for areal specialization[53]. HVA neurons receiving direct V1 input may exhibit higher NCs with V1, because direct synaptic connectivity is a source of NCs[51]. Our results indicated that tuning group-specific differences in NCs, suggesting that the two pathways could contribute to functional specialization. In the low TF and medium SF tuning group (Group 2) PM exhibited extremely high correlation with V1 (**Fig. 3e**). PM did not respond to this frequency band as strongly as V1 and the other two HVAs (**Fig. 3b**). These results may indicate that V1 input is important for the tuning of this frequency band in PM. On the contrary, PM responded stronger to the low TF and high SF band (Group 3) than LM and AL, and similarly with V1, but the direction encoding

in PM was not comparable with that of V1 (**Fig. 3b, d**). Moreover, PM neurons of this tuning group exhibited extremely high correlation within the area itself (**Fig. 3e**). These results suggested that a V1 independent pathway may play a large role in the formation of this tuning group in PM. In addition, AL exhibited high NCs within itself to high TF and low SF gratings, and exhibited strong interactions with V1 to high TF and medium SF gratings. Both frequency bands were well represented in AL, but may formed through different pathway, that the former relays on a V1-independent pathway, while the latter may relay through a V1-dependent pathway. Together, these findings suggest that the generation of specific tuning groups in AL and PM are partially relayed on the projections from V1 neurons with non-overlapping frequency preference, *i.e.* a low TF-medium SF preference V1 population is projected into PM, while a high TF-medium SF V1 population is projected into AL[38]. Nevertheless, V1 exhibited broad functional interactions with three HVAs studied here, which is consistent with recent anatomical findings that the majority V1 neurons projected to more than one HVAs[36].

While these findings can shed light on the emergence of tuning properties in HVAs, it remains unclear what adaptive behaviors these tuning properties support. Ultimately, that is what is selected for in evolution, and it will require thorough examinations of neuroethologically relevant behaviors, together with multi-brain region analysis as done in this study, to uncover insights on that subject.

Online Methods

Animal and surgery

All animal procedures and experiments were approved by the institutional Animal Care and Use Committee of University of North Carolina at Chapel Hill and carried out in accordance with the regulation of the US Department of Health and Human Services. GCaMP6s expressing transgenic adult mice of both sex were used in this study. Mice were 110~300 days old for data collection. GCaMP6s expressing were induced by triple crossing of TITL-GCaMP6s line (Allen Institute Ai94), Emx1-Cre line (Jackson Labs #005628) and ROSA:LNL:tTA line (Jackson Labs #011008)[43]. Mice were housed under a 12-h/12-h light-dark cycle, and experiments were performed during the dark cycle of mice. Mice were anesthetized with isoflurane (1.5~1.8%) and acepromazine (1.5~1.8 mg/kg body weight) when perform visual cortex craniotomy. Carpofen (5 mg/kg body weight) was administered prior to surgery. Mice body temperature were maintained using physically activated heat packs during surgery. Mouse eyes were kept moist with ointment during surgery. The scalp overlaying the right visual cortex was removed, and a custom head-fixing imaging chamber with 5-mm diameter opening was mounted to the skull with cyanoacrylate-based glue (Oasis Medical) and dental acrylic (Lang Dental). A 4-mm diameter craniotomy was performed over visual cortex and covered with #1 thickness coverslip.

Locate visual areas by intrinsic signal optical imaging (ISOI)

ISOI experiments were carried out similarly as previously[30,45,54]. Briefly, the pial vasculature images and intrinsic signal images were collected using CCD camera (Teledyne DALSA 1M30) at the craniotomy window. A 4.7 × 4.7 mm^2 cortical area was imaged at 9.2 µm/pixel spatial resolution and at 30 Hz frame rate. The pial vasculature was illuminated and captured through green filters (550 ± 50 nm and 560 ± 5 nm, Edmund Optics). The ISO image was collected by focusing 600 µm down from the pial surface. The intrinsic signals were illuminated and captured through red filters (700 ± 38 nm, Chroma and 700 ± 5 nm, Edmund Optics). Custom ISOI instrument were adapted from Kalatsky and Stryker[55]. Custom acquisition software for ISOI imaging collection was adapted from David Ferster[30]. During ISOI, mice were 20 cm from a flat monitor (60 × 34 cm^2), which covers the visual field (110° x 75°) of the left eye. Mice were lightly anesthetized with isoflurane (0.5%) and acepromazine (1.5–3 mg/kg). The body temperature was maintained at 37 °C using custom electric heat pad[30]. Intrinsic signal response to vertical and horizontal drifting bar was used to generate azimuth and elevation retinotopic maps (Fig. 1b). The retinotopic maps were then used to locate V1 and HVAs (Fig. 1b). Borders between these areas were drawn at the meridian of elevation and azimuth retinotopy manually[32,45]. The vasculature map then provided landmarks to identify visual areas in two-photon imaging.

In vivo Two-photon imaging

Two-photon imaging was carried out using custom Trepan2p microscope controlled by costume LabView software[30]. Two-region imaging was achieved by laser beam split and temporal multiplexing[30]. Briefly, two-photon excitation light from an 80 MHz Newport Spectra-Physics Mai Tai DeepSee laser was split into two beams through polarized optics, and one path is delayed 6.25 ns relative to the other. The two beams were imparted by custom-motorized steering mirrors and tunable lenses independently, such that the X, Y, Z plane of the two paths can be independently positioned in the full field (4.4 mm diameter) positioned during imaging. Both beams were scanned by resonant scanner (4 kHz, Cambridge Technologies), and simple photon signal was collected by PMT (H7422P-40, Hamamatsu). In the current study, two-photon imaging of 500 x 500 μm^2 was collected at 13.3 Hz for two-region imaging, or 6.67 Hz for quartic-region imaging. Imaging was performed with about <80 mW excitation 910 nm laser out of the front of the objective (0.45 NA). Mice were recovered in home cage for at least 2 days before acquiring two-photon imaging, after surgery. Mice were head-fixed at about 11 cm from a flat monitor, with their left eye facing the monitor, during imaging. A 70° x 45° the left visual field was covered. If not otherwise stated, two-photon images were recorded from quite

awake mice. For anesthetized experiments in supplementary fig. 3c, d, mice were lightly anesthetized under 1% isoflurane. During two-photon imaging, we monitor mouse pupil position and diameter using custom-controlled CCD camera (GigE, National Instruments) at 20~25 fps. No additional light stimulation was used for pupil imaging.

Visual stimuli

Visual stimulation was displayed on 60 Hz LCD monitor (9.2 x 15 cm^2). All stimuli were displayed in full contrast, and in red color cannel of the monitor to minimize the cross talk with the two-photon imaging. For course population RF and single neuron RF mapping (Fig 1, supplementary fig 1), a rectangular (7.5° x 8.8°) bright moving patch containing vertical drifting grating (2Hz, 0.05 cpd) on a dark background was displayed. The moving patch was appeared and disappear on a random position of the full monitor in pseudo random order without interruption by a gray screen, and presented on each position for 5 sec.

To characterized the value and structure of correlation, as well as tuning properties of V1 and HVAs (**Fig. 2-4**), we showed mice full screen sine-wave drifting grating stimuli is 8 directions (0 – 315°, in 45° step), with a of 0.02, 0.05 or 0.19 cpd, and a TF of 1, 2 or 8 Hz (72 conditions in total). Each of the sine-wave drifting grating stimuli was presented for 2 s in pseudo random order. Stimuli with the same SF and TF was presented successively without interruption. A gray screen was presented for 3 s when changing the SF and TF of stimuli. We also characterized the noise correlation structure to naturalistic videos (**Fig. 2, 4**). Two naturalistic videos of navigating a mouse home cage was shown. Each lasted for 32 secs.

For estimation correlation with regularized models (**Fig. 5**, **Supplementary Fig. 11**), we used two following stimuli: (1) drifting gratings with 3 directions (60°, 80°, 90°) at 0.05 cpd and 2 Hz (3 conditions); (2) sine-wave upward motion grating at a SF of 0.02, 0.05 or 0.19 cpd, and a TF of 1, 2 or 8 Hz (9 conditions). For both stimuli, gratings were presented for 1.5 sec in pseudo random order. For stimulus (1), 1 s gray screen was shown after every 9 grating stimuli. For stimulus (2), the contrast of the sine-wave grating stimulus ramp up from 0% to 100% within 0.3 s, and then ramp down from 100% to 0% within 0.3 s.

Calcium imaging processing

Calcium imaging processing was carried out using custom MATLAB codes. Two-photon calcium imaging was motion corrected using Suit2p subpixel registration module[56]. Neuron ROIs and cellular calcium traces were extracted from imaging stacks using custom code adapted from Suit2p modules[56]. Neuropil contamination was corrected by subtracting the common time series (1st principal component) of a spherical surrounding mask of each neuron from the cellular calcium traces[31,57]. Neuropil contamination corrected calcium traces were then deconvolved using a Markov chain Monte Carlo (**MCMC**) methods[57,58]. For each calcium trace, we repeated the MCMC simulation for 400 times, and measured the signal-to-noise of MCMC spike train inference for each cell (**Supplementary Fig. 1a**). For all subsequent analysis, only cells that reliable spike train inference results were included.

Receptive field, sparseness and reliability

We mapped RFs by reverse correlation of neuronal responses with the locations of the moving patch of drifting grating stimulus. For population RF mapping, population neuronal responses of simultaneously recorded neurons from a 500 x 500 μm^2 imaging window were reverse correlated with the stimulus locations.

To quantify reliability, we computed trial-to-trial Pearson correlations for neuronal responses (500 ms time bins) to each stimulus type. The lifetime sparseness was the equation 1[59].

Sparseness to sine-wave gratings was computed using 2 s time bins (**Fig. 2a**). While the sparseness to naturalistic videos was computed using 500 ms bin (**Fig. 2a**). We quantified the sparseness of reliably firing neurons (reliability > 0.08). The binning size did not affect the qualitative results of reliability and sparseness.

Correlation calculation

Noise correlation was defined as the trial-to-trial correlation of residual spike count (1 s time window, if not otherwise stated) after subtracting the mean response to each stimulus. Residual spike count to all stimuli (eg. gratings with different directions and SFs and TFs), and all trials were concatenated into one column vector per neuron (u_i, i = 1,2…N, neuron identity). The noise correlation r_{sc} was computed as the Pearson correlation of u_i and u_j.

In **Fig. 3e**, we computed the normalized noise correlation by subtracting the mean of the population noise correlation and divided the standard deviation of the population noise correlation.

For characterizing noise correlation structure to sine-wave grating (72 conditions) (**Fig. 2-4**, supplementary fig. 2-10) and naturalistic videos, we collected 10~20 trials for each condition. For modeling correlation and estimation partial correlation (**Fig 5, Supplementary Fig 11**), we collected about 240~300 trials/condition for the 3 directions drifting grating stimuli (3 conditions) and collected 80~100 trials/condition for the upward motion drifting grating stimuli (9 conditions).

Signal correlation was defined as the neuron-to-neuron Pearson correlation of mean responses. Mean response was a 72-element column vector, computed by trial averaging responses to sine-wave gratings with 72 conditions (**Fig 2-4, Supplementary Fig. 4**).

To examine the relation between noise correlation and joint firing rate between a pair of neurons. We computed the mean joint spike count (geometric mean spike count average over all stimuli (eg. 72 conditions for sine-wave drifting gratings) and the peak joint spike count (maximal geometric mean spike count) of individual neuron pairs.

To compare the noise correlation between areas fairly, we computed the population mean noise and signal correlations with a subset of neurons from each areas so that the distribution of the mean joint spike count of neuron pairs of one visual areas matches with another[12], after excluding a subset of neuron pairs with extremely low joint spike count (mean joint spike count < 0.02 sp/s) and low reliability (< 0.08). Population with fewer than 50 neuron pairs after mean matching were excluded. Also, for computing the noise correlation of a distance bin, or a signal correlation bin, data points with fewer than 50 neuron pairs were excluded.

We computed inter-area NCs with simultaneously recorded regions that shared greater than 40% of population RF. We kept this criterion even though we did not detect a relationship between the inter-area NC and the fraction of population RF overlap within the tested range (p = 0.37; **Supplementary Fig. 1e**).

Significance of noise correlation

Since the value of noise correlations was small, we tested whether these values were significantly above zero. We compared the noise correlation with trial-shuffled noise correlation, the latter was computed using trial-shuffled data (the order of trials were randomized for each neuron independently). The population mean noise correlation computed with trial-aligned data was significantly higher than that of the trial-shuffled data with the size of experimental population (**Fig. 2b, c**).

Accuracy of noise correlation

We investigated the accuracy of noise correlation estimation with both data and model. The individual noise correlations of the same set of neurons varied when computing using different random sub set of trials (**Supplementary Fig. 2a**). We computed the population mean value of noise correlation of random subset of neuron pairs and calculated the confidence interval for estimating the population mean noise correlation. The accuracy of population mean estimation increases with the number of neurons, even with limited number of trials (**Supplementary Fig. 2b**). We further characterized the estimation accuracy by simulating correlated neuron population[60], which allows arbitrary number of trials. The expected firing rate and expected population mean correlation matches our experimental data. To achieve an accurate estimation (1/10 standard error/mean value) of population mean correlation converges with >100 neurons even using experimental level trial numbers (**Supplementary Fig. 2d**).

Tuning properties

Gaussian mixture model

Trial-averaged population responses to sine-wave grating stimuli (72 conditions) were first denoised and reduced dimension by principle component analysis (PCA). To characterize the tuning properties unbiasedly, neurons were classified using Gaussian mixture model[61] (**GMM**) of the first 45 PCs of population response. We kept 45 PCs for two reasons. First, the first 45 PCs captured >85% of the variance of population data (**Supplementary Fig. 7a**). Second, population neuron firing was well predicted by the first 45 PCs (**Supplementary Fig. 7a**). We also tested a wide range number of PCs (20~70), and we found the tuning group clustering was not affected by the number of PCs. Neurons collected from different visual areas and different animals were pool together in training GMM (8988 neurons in total). GMM with 65 classes was selected based on Bayesian information criterion (BIC) (**Supplementary Fig. 7b**). We also examined model with smaller (20, 30 and 45) or even larger number of classes (75), the overall results held regardless of the number of GMM classes. Neurons with similar tuning properties were classified as the same class. **Supplementary Fig. 5** shows the tuning property of all 65 GMM classes. We manually organized the 65 GMM classes into 6 groups based on their preferred SF, TF (**Fig. 3a**). Group 1 prefers low SF and low TF (LSLT, 0.02 cpd, 1-2 Hz), group 2 prefers medium SF and low TF (MSLT, 0.05 cpd, 1-2 Hz), group 3 prefers high SF low TF (HSLT, 0.19 cpd, 1-2 Hz), group 4 prefers low SF high TF (LSHT, 0.02 cpd, 8 Hz), group 5 prefers medium SF and high TF (MSHT, 0.05 cpd, 8 Hz), group 6 prefers high SF and high TF (HSHT, 0.19 cpd, 8 Hz) and group 7 not specific. Group 7 included 4 classes which did not exhibit specific response features, among them two classes are extremely small (each contains <5 neurons), and the other two contains neurons with small response strength (mean spike count < 0.5 spikes/s to preferred stimulus). As we have been inclusive in data selection for the GMM training and included two firing neurons, the latter two classes contain about 1500 neurons in total. It is justifiable to exclude low response neurons from further analysis. Thus, the whole group 7 was excluded for further analysis. The size of each class was shown in supplementary fig. 6a.

Orientation and direction selectivity

Majority GMM classes of group 1-6 are direction selective. Only class 5 in group 2 and 56 in group 3 have ambiguous direction selectivity (**Supplementary Fig. 5**). The preferred directions were computed as averaging responses to its preferred direction of each neuron within a tuning group or within a local area, and normalized to one (**Supplementary Fig. c, d)**. For neurons with high direction selectivity, neuron responses to preferred direction was considered, while for neurons with low direction selectivity (DSI < 0.5), neuron responses to both preferred and null directions were included.

Direction selectivity index and orientation selectivity index were computed using following equations.

GMM classification accuracy

We examined the accuracy of GMM classification. We performed GMM clustering on 10 random subsets of neurons (90% of all neurons). We found the center of the Gaussian profile of each class was consistent (supplementary fig. 8d). The same class of different GMM was identified by match the center of class. Then we asked whether a neuron was classified in the same class in each GMM model. We found neurons were consistently classified into the same class in GMMs of random subset of data (S**upplementary Fig. 7c**). We also performed GMM on population data after randomly shuffling neuron identity (10 permutation). Classes were identified by matching the center of class, and then grouped following the previous definition. We found that neurons are allocated into the same group in GMMs of random ordered data (S**upplementary Fig. 7e, f**). These analyses suggested that GMM provided reliable classification of neurons.

ISOI warping

We spatially registered ISOI map of V1 to align with that of LM. We first segmented the ISOI map by color segmentation using kmeans clustering, and then determined the center of

each color segment. Then we performed the affine transformation of color band centers of V1 to match that of LM. The transformation matrix M was determined by minimizing the distance between transformed V1 centers and LM centers using Matlab function *fminsearch*.

References

1. Wang, Q. & Burkhalter, A. Area Map of Mouse Visual Cortex. *J. Comp. Neurol.* **502,** 339–357 (2007).
2. Chiang, A. S. *et al.* Three-dimensional reconstruction of brain-wide wiring networks in drosophila at single-cell resolution. *Curr. Biol.* **21,** 1–11 (2011).
3. Oh, S. W. *et al.* A mesoscale connectome of the mouse brain. *Nature* **508,** 207–214 (2014).
4. Cohen, M. R. & Kohn, A. Measuring and interpreting neuronal correlations. *Nat. Neurosci.* **14,** 811–819 (2011).
5. Shadlen, M. N. & Newsome, W. T. The Variable Discharge of Cortical Neurons : Implications for Connectivity , Computation , and Information Coding. *J. Neurosci.* **18,** 3870–3896 (1998).
6. Rabinowitz, N. C., Goris, R. L., Cohen, M. & Simoncelli, E. P. Attention stabilizes the shared gain of V4 populations. *Elife* 1–24 (2015).
7. Hofer, S. B. *et al.* Differential connectivity and response dynamics of excitatory and inhibitory neurons in visual cortex. *Nat. Neurosci.* **14,** 1045–1052 (2011).
8. Middleton, J. W., Omar, C., Doiron, B. & Simons, D. J. Neural Correlation Is Stimulus Modulated by Feedforward Inhibitory Circuitry. *J. Neurosci.* **32,** 506–518 (2012).
9. Ecker, A. S. *et al.* State Dependence of Noise Correlations in Macaque Primary Visual Cortex. *Neuron* **82,** 235–248 (2014).
10. Renart, A. *et al.* The asynchronous state in cortical circuits. *Science* **327,** 587–590 (2010).
11. Ocker, G. K. *et al.* From the statistics of connectivity to the statistics of spike times in neuronal networks. *Curr. Opin. Neurobiol.* **46,** 109–119 (2017).
12. Churchland, M. M. *et al.* Stimulus onset quenches neural variability: a widespread cortical phenomenon. *Nat. Neurosci.* **13,** 369–378 (2010).
13. Dadarlat, M. C. & Stryker, M. P. Locomotion Enhances Neural Encoding of Visual Stimuli in Mouse V1. *J. Neurosci.* **37,** 3764–3775 (2017).
14. Rose, T., Jaepel, J., Hübener, M. & Bonhoeffer, T. Cell-specific restoration of stimulus preference after monocular deprivation in the visual cortex. *Science* **352,** 1319–1322 (2016).
15. Reimer, J. *et al.* Pupil Fluctuations Track Fast Switching of Cortical States during Quiet Wakefulness. *Neuron* **84,** 355–362 (2014).
16. Poulet, J. F. A. & Petersen, C. C. H. Internal brain state regulates membrane potential synchrony in barrel cortex of behaving mice. *Nature* **454,** 881–885 (2008).
17. Litwin-kumar, A. & Doiron, B. Slow dynamics and high variability in balanced cortical networks with clustered connections. *Nat. Neurosci.* **15,** 1498–1505 (2012).
18. Stringer, C. *et al.* Inhibitory control of correlated intrinsic variability in cortical networks. *Elife* **5,** 1–33 (2016).
19. Lin, I. C., Okun, M., Carandini, M. & Harris, K. D. The Nature of Shared Cortical Variability. *Neuron* **87,** 645–657 (2015).
20. Ecker, A. S., Denfield, G. H., Bethge, M. & Tolias, A. S. On the Structure of Neuronal Population Activity under Fluctuations in Attentional State. *J. Neurosci.* **36,** 1775–1789 (2016).
21. Law, C.-T. T. & Gold, J. I. Reinforcement learning can account for associative and perceptual learning on a visual-decision task. *Nat. Neurosci.* **12,** 655–663 (2009).
22. Rosenbaum, R., Smith, M. A., Kohn, A., Rubin, J. E. & Doiron, B. The spatial structure of correlated neuronal variability. *Nat. Neurosci.* **20,** 107–114 (2017).
23. Smith, M. A. & Sommer, M. A. Spatial and Temporal Scales of Neuronal Correlation in Visual Area V4. *J. Neurosci.* **33,** 5422–5432 (2013).
24. Smith, M. A. & Kohn, A. Spatial and Temporal Scales of Neuronal Correlation in Primary Visual Cortex. *J. Neurosci.* **28,** 12591–12603 (2008).
25. Huang, C. *et al.* Circuit-based models of shared variability in cortical networks. *BioRxiv* (2017). doi: 10.1101/217976
26. Ruff, X. D. A. & Cohen, X. M. R. Attention Increases Spike Count Correlations between Visual Cortical Areas. *J. Neurosci.* **36,** 7523–7534 (2016).
27. Ruff, X. D. A. & Cohen, X. M. R. Stimulus Dependence of Correlated Variability across Cortical Areas. *J. Neurosci.* **36,** 7546–7556 (2016).

28. Ruff, D. A. & Cohen, M. R. A normalization model suggests that attention changes the weighting of inputs between visual areas. *Proc. Natl. Acad. Sci.* 4085–4094 (2017). doi:10.1073/pnas.1619857114
29. Schaffelhofer, S. & Scherberger, H. Object vision to hand action in macaque parietal , premotor , and motor cortices. *Elife* 1–24 (2016).
30. Jeffrey N. Stirman, Ikuko T. Smith, Michael W. Kudenov, S. L. S. Wide field-of-view, multi-region two-photon imaging of neuronal activity. *Nat. Biotechnol.* **34,** 857–862 (2016).
31. Andermann, M. L., Kerlin, A. M., Roumis, D. K., Glickfeld, L. L. & Reid, R. C. Functional Specialization of Mouse Higher Visual Cortical Areas. *Neuron* **72,** 1025–1039 (2011).
32. Marshel, J. H., Garrett, M. E., Nauhaus, I. & Callaway, E. M. Functional specialization of seven mouse visual cortical areas. *Neuron* **72,** 1040–1054 (2011).
33. Zhuang, J. *et al.* An extended retinotopic map of mouse cortex. *Elife* **6,** 1–29 (2017).
34. Vries, S. E. J. de *et al.* A large-scale, standardized physiological survey reveals higher order coding throughout the mouse visual cortex. *bioRxiv* 359513 (2018). doi:10.1101/359513
35. Glickfeld, L. L., Andermann, M. L., Bonin, V. & Reid, R. C. Cortico-cortical projections in mouse visual cortex are functionally target specific. *Nat. Neurosci.* **16,** 219–26 (2013).
36. Han, Y. *et al.* The logic of single-cell projections from visual cortex. *Nature* **556,** 51 (2018).
37. Wang, Q., Sporns, O. & Burkhalter, A. Network Analysis of Corticocortical Connections Reveals Ventral and Dorsal Processing Streams in Mouse Visual Cortex. *J. Neurosci.* **32,** 4386–4399 (2012).
38. Kim, M., Znamenskiy, P., Iacaruso, M. F. & Mrsic-flogel, T. D. Exclusive functional subnetworks of intracortical projections neurons in primary visual cortex. *bioRxiv* (2017).
39. Berezovskii, V. K., Nassi, J. J. & Born, R. T. Segregation of feedforward and feedback projections in mouse visual cortex. *J. Comp. Neurol.* **519,** 3672–3683 (2011).
40. D'Souza, R. D., Meier, A. M., Bista, P., Wang, Q. & Burkhalter, A. Recruitment of inhibition and excitation across mouse visual cortex depends on the hierarchy of interconnecting areas. *Elife* **5,** 1–19 (2016).
41. Harris, K. D. & Shepherd, G. M. G. The neocortical circuit: themes and variations. *Nat. Neurosci.* **18,** 170–181 (2015).
42. Seabrook, T. A., Burbridge, T. J., Crair, M. C. & Huberman, A. D. Architecture, Function, and Assembly of the Mouse Visual System. *Annu. Rev. Neurosci.* **40,** 499–538 (2017).
43. Madisen, L. *et al.* Transgenic Mice for Intersectional Targeting of Neural Sensors and Effectors with High Specificity and Performance. *Neuron* **85,** 942–958 (2015).
44. Chen, T. W. *et al.* Ultrasensitive fluorescent proteins for imaging neuronal activity. *Nature* **499,** 295–300 (2013).
45. Smith, I. T., Townsend, L. B., Huh, R., Zhu, H. & Smith, S. L. Stream-dependent development of higher visual cortical areas. *Nat. Neurosci.* **20,** 200–208 (2017).
46. Garrett, M. E., Nauhaus, I., Marshel, J. H. & Callaway, E. M. Topography and Areal Organization of Mouse Visual Cortex. *J. Neurosci.* **34,** 12587–12600 (2014).
47. Schulz, D. P. A., Sahani, M. & Carandini, M. Five key factors determining pairwise correlations in visual cortex. *J. Neurophysiol.* **114,** 1022–1033 (2015).
48. Ecker, A. S. *et al.* Decorrelated Neuronal Firing in Cortical Microcircuits. *Science* **327,** 584–586 (2010).
49. Kohn, A. & Smith, M. A. Stimulus Dependence of Neuronal Correlation in Primary Visual Cortex of the Macaque. *J. Neurosci.* **25,** 3661–3673 (2005).
50. Ko, H. *et al.* The emergence of functional microcircuits in visual cortex. *Nature* **496,** 96–100 (2013).
51. Ko, H. *et al.* Functional specificity of local synaptic connections in neocortical networks. *Nature* **473,** 87–91 (2011).
52. Han, X., Vermaercke, B. & Bonin, V. Segregated encoding of spatiotemporal features in the. *bioRxiv* 1–38 (2018).
53. Tohmi, M., Meguro, R., Tsukano, H., Hishida, R. & Shibuki, K. The extrageniculate visual pathway generates distinct response properties in the higher visual areas of mice. *Curr. Biol.* **24,** 587–597 (2014).
54. Smith, S. L. & Häusser, M. Parallel processing of visual space by neighboring neurons in mouse visual cortex. *Nat. Neurosci.* **13,** 1144–1149 (2010).
55. Kalatsky, V. A., Stryker, M. P. & Foundation, W. M. K. New paradigm for optical imaging: Temporally encoded maps of intrinsic signal. *Neuron* **38,** 529–545 (2003).

56. Pachitariu, M. *et al.* Suite2p: beyond 10,000 neurons with standard two-photon microscopy. *bioRxiv* 061507 (2016). doi:10.1101/061507
57. Harris, K. D., Quiroga, R. Q., Freeman, J. & Smith, S. L. Improving data quality in neuronal population recordings. *Nat. Neurosci.* **19,** 1165–1174 (2016).
58. Pnevmatikakis, E. A., Merel, J., Pakman, A. & Paninski, L. Bayesian spike inference from calcium imaging data. *Adv. Neural Inf. Process. Syst.* **26,** 1250–1258 (2013).
59. Froudarakis, E. *et al.* Population code in mouse V1 facilitates readout of natural scenes through increased sparseness. *Nat. Neurosci.* **17,** 851–857 (2014).
60. Macke, J. H., Berens, P., Ecker, A. S., Tolias, A. S. & Bethge, M. Generating Spike Trains with Specified Correlation Coefficients. *Neural Comput.* **21,** 397–423 (2009).
61. Baden, T. *et al.* The functional diversity of retinal ganglion cells in the mouse. *Nature* **529,** 345–350 (2016).

s